RESEARCH ARTICLE

NANO · MICRO small
www.small-journal.com

A Function-Oriented Binder with Exceptional Interface Ion Transport and Impurity Tolerance for Hard Carbon Anode

Xinyu Qiao, Guobiao Jin, Rui Liu, Jiyang Hou, Xinlin Shi, Lu Wang, Qimin Tian, Hongzhou Lu, Zhihao Shen, Yumeng Lan, Zirui Lou, and Feng Pan**

Hard carbon is the sole anode material employed in commercial sodium-ion batteries. However, its intrinsic defects and impurities will lead to battery failure, diminishing further development of sodium batteries in energy storage. Here, an acrylonitrile copolymer and poly(ethylene oxide) (LA/PEO) composite binder is developed to address these challenges in biomass-derived hard carbon. Typical commercial biomass-derived hard carbon with this binder (HC-LA/PEO) achieved an initial coulombic efficiency (ICE) of 91.1% and a reversible capacity of 341.12 mAh g^{-1}, superior to most of binders currently used. When transition metal ion impurities exist in hard carbon, the HC-LA/PEO shows better tolerance and even shows a higher reversible capacity than its high purity counterpart. After function-oriented design, due to hydrogen bonding and polar interaction, the HC-LA/PEO demonstrated superior initial efficiency and reversible capacity while enhancing mechanical strength and reducing electrode brittleness. In addition, this composite binder induced a more uniform and stable SEI layer on hard carbon, improving interfacial stability and ion transport efficiency. The LA/PEO binder acts as an intelligent gatekeeper mitigating the adverse effects from intrinsic defects and impurities, consequently, gives full play to the biomass-derived hard carbon in sodium batteries.

1. Introduction

Sodium-ion batteries (SIBs) are emerging as an effective alternative to lithium-ion batteries (LIBs) due to the abundance, low cost, and wide availability of sodium.[1] Although SIBs have a lower energy density, they are particularly suitable for large-scale grid energy storage and low-speed electric vehicles.[2–5] Due to the larger ionic radius of sodium compared to lithium, these batteries require anode materials that can accommodate sodium ions, unlike the graphite commonly used in lithium-ion batteries. Within the same carbon-based system, SIBs predominantly use amorphous carbon as anode materials. Hard carbon (HC), with its high specific capacity and low expansion coefficient, has become a recognized anode material for SIBs.[6–9]

The main precursors for HC include resin-based, biomass-based, and pitch-based materials. Among these, biomass-derived HC exhibits significant advantages due to its high specific capacity and low cost.[8,9] However, the intrinsic defects and impurities in biomass-derived HC can lead to decreased conductivity and structural instability in practical applications. These problems not only reduce the initial Coulombic efficiency (ICE) but also affect the overall performance and lifespan of the battery during cycling.[10–13]

Currently, most research on biomass-derived HC materials has focused on modifying the active materials and optimizing electrolyte compatibility, but relatively few investigation has been conducted into binders, which serve as the intermediate substances between the active material and the electrolyte.[14,15] As a critical component in the anode, the binder, though constituting less than 5–10% of the material, acts as a "gatekeeper" for the insertion and extraction of sodium ions into the HC material, directly impacting the overall performance and stability of the battery.[9,12,16]

Binders can be classified into water-based and oil-based types based on their solubility in different solvent systems. The solvents required for oil-based systems often have toxicity and harmful effects, posing environmental and health risks.[15,17] Consequently, research on HC anode binders predominantly centers around developing novel binders, such as polymer-sol binders, nanofiber binders, and polymer-companion binders, or on developing non-toxic, cost-effective, and easily-handled water-based binders.[18–20] A proper binder can facilitate the formation of a uniformly stable solid electrolyte interface (SEI) film on the surface of HC, thereby enhancing the cycling stability of the anode.[3–4] However, existing research lacks extensive comparison of commercially available binders suitable for HC and explores solutions for practical issues caused by natural impurities.[15,21]

X. Qiao, G. Jin, R. Liu, X. Shi, L. Wang, Q. Tian, H. Lu, Z. Shen, Y. Lan, Z. Lou, F. Pan
School of Advanced Materials
Peking University Shenzhen Graduate School
Shenzhen 518055, P. R. China
E-mail: zrlou@pku.edu.cn; panfeng@pkusz.edu.cn
J. Hou
State Key Laboratory of Heavy Oil Processing
China University of Petroleum
Changping, Beijing 102249, P. R. China

The ORCID identification number(s) for the author(s) of this article can be found under https://doi.org/10.1002/smll.202500532

DOI: 10.1002/smll.202500532

To address the deficiencies of existing research and drawing from the experience of suppressing the dissolution of transition metal ions in lithium cobalt oxide batteries, this study design a novel water-based binder based on acrylonitrile copolymer and poly(ethylene oxide) (LA/PEO) to evaluate its synergistic effects with HC in SIBs.[22–26] This study highlights the comparative advantages of LA/PEO over traditional commercial binders and has achieved favorable results when compared to the best-performing binder CMC/SBR, exploring its potential to promote the ion conduction of the binder itself and the formation of a more uniform and stable SEI layer. Furthermore, to tackle practical issues, considering the potential metal impurities in biomass-derived HC and the affinity of the cyano group in the LA/PEO binder for various metal ions,[27,28] we furthered our comparative analysis by doping the HC with metal impurities. The research results show that the batteries assembled with the low-cost LA/PEO binder exhibit outstanding capacity enhancement, improved rate performance, favorable high and low temperature performances, and impurity tolerance. This work holds great promise for the future development of SIBs as it provides a novel water-based binder with excellent performance, opening up new avenues for improving battery efficiency and stability, and potentially leading to more advanced and reliable energy storage solutions.

2. Results and Discussion

The study delves into the intrinsic defects and impurity content of biomass-derived HC and their impact on the performance of SIBs, especially their electrochemical properties and cycle stability. Given the potential application of HC materials in sodium-ion battery anodes, this research employs a commercial LA133 binder (referred to as LA), which has been widely used in both anode and cathode materials of LIBs. The LA binder contains functional groups such as acrylamide and lithium carboxylate, which have been shown to form a stable interface with HC, facilitating effective sodium ion transport.[24,29] Additionally, the LA binder contains highly polar cyano groups, which can effectively suppress the dissolution of metal impurity ions, thereby enhancing the overall performance of the battery.[30]

Nevertheless, when LA is used as the sole binder, despite its decent electrochemical performance, its linear structure leads to brittleness, causing the prepared electrodes to fracture easily during the coating process, thus limiting its practical application.[31] To address this issue, this study introduces a certain proportion of polyethylene oxide (PEO) into LA to prepare an LA/PEO composite binder (LA:PEO = 9:1) (Figure S1, Supporting Information). The selection of the basic components of LA and PEO binders is founded on the functions of diverse groups. The carboxylic acid group and amide group act as anchor points, enabling it to be closely combined with the hard carbon interface and enhancing the adhesion effect. The amide group is beneficial for constructing a hydrogen bond cross-linked network structure, and its decomposition products can facilitate the generation of the inorganic component NaF.[32] The cyano group offers polar interaction to stabilize the structure and can also restrain the dissolution of impurity metal ions in the hard carbon bulk phase. PEO can ameliorate the brittleness of LA and boost the sodium ion transport rate. However, common commercial binders (such as PVDF, CMC, CMC/SBR, etc.) usually carry groups that can only provide one or two of the above-mentioned functions (**Scheme 1**). This composite binder forms a crosslinked network structure via hydrogen bonding and polar interactions between the two polymers, remarkably enhancing the mechanical toughness of the electrodes and possessing the ability to form a thin and robust SEI film.[22,33]

For ease of description, the HCs treated with different binders are designated as HC-LA/PEO, HC-CMC, HC-PVDF, and HC-CMC/SBR. In the current research on hard carbon, there is a paucity of data regarding HC-CMC/SBR. Consequently, within the main text, our primary focus will be on comparing HC-LA/PEO, which is prevalently utilized in laboratory investigations, with HC-CMC and HC-PVDF. Nevertheless, considering the extensive application of HC-CMC/SBR in industrial settings and the persisting doubts surrounding whether novel binders can surpass CMC/SBR across all performance metrics, we have carried out pertinent tests on HC-CMC/SBR, and the resultant data has been incorporated into the supplementary materials.[8] Preliminary electrochemical performance evaluation of HC-LA/PEO revealed an ICE of up to 91.1% at a current density of 0.03 A g^{-1}, with an initial reversible capacity of 341.12 mAh g^{-1}. This performance surpasses that of HC-CMC (88.7%, 308.68 mAh g^{-1}) and HC-PVDF (72.7%, 314.06 mAh g^{-1}) (**Figure 1a**; Figure S2, Supporting Information). In rate capability tests, HC-LA/PEO exhibited excellent performance across all test rates, particularly under high-rate charge–discharge conditions, where its capacity decay rate was significantly lower than other binders (Figure 1b). After activation at 0.03 A g^{-1}, HC-LA/PEO displayed a high capacity retention rate of 97.37% in long-cycle tests at 0.6 A g^{-1}, with a reversible capacity of 295.20 mAh g^{-1} at the 300th cycle. In comparison, HC-CMC and HC-PVDF showed capacity retention rates of 96.19% and 96.02%, along with reversible capacities of 261.84 and 239.69 mAh g^{-1}, respectively (Figure 1c). By analyzing electrochemical impedance spectroscopy (EIS) and galvanostatic intermittent titration technique (GITT) results, we gained a deeper understanding on advantages of the LA/PEO composite binder. EIS tests showed that HC electrodes using LA/PEO binder had lower charge transfer resistance and better electronic conductivity. The low and less variable resistance value indicates efficient and stable electron transfer at the electrode interface, which is crucial for high-performance batteries (Figure 1d; Figure S3, Supporting Information). GITT tests provided quantitative data on ion diffusion coefficients and ion transport properties of electrode materials, showing a significant advantage of HC-LA/PEO electrodes in sodium-ion diffusion efficiency. This implies smoother ion transport channels on the HC surface, enhancing the battery's charge–discharge performance (Figure 1e; Figures S4 and S5, Supporting Information).[9,24] Further cyclic voltammetry (CV) tests demonstrate that HC-LA/PEO exhibits remarkable advantages. The relatively high peak current absolute value indicates a high level of electrode reaction activity and rate. The high forward rate implies that during the forward scan, ions can rapidly diffuse from the bulk solution to the electrode surface, facilitating the rapid progress of the electrode reaction. This is highly beneficial for the battery charging process, as it enables the completion of a large amount of charge transfer in a short time, thus enhancing the charging efficiency. Simultaneously, the high reverse rate indicates that during the

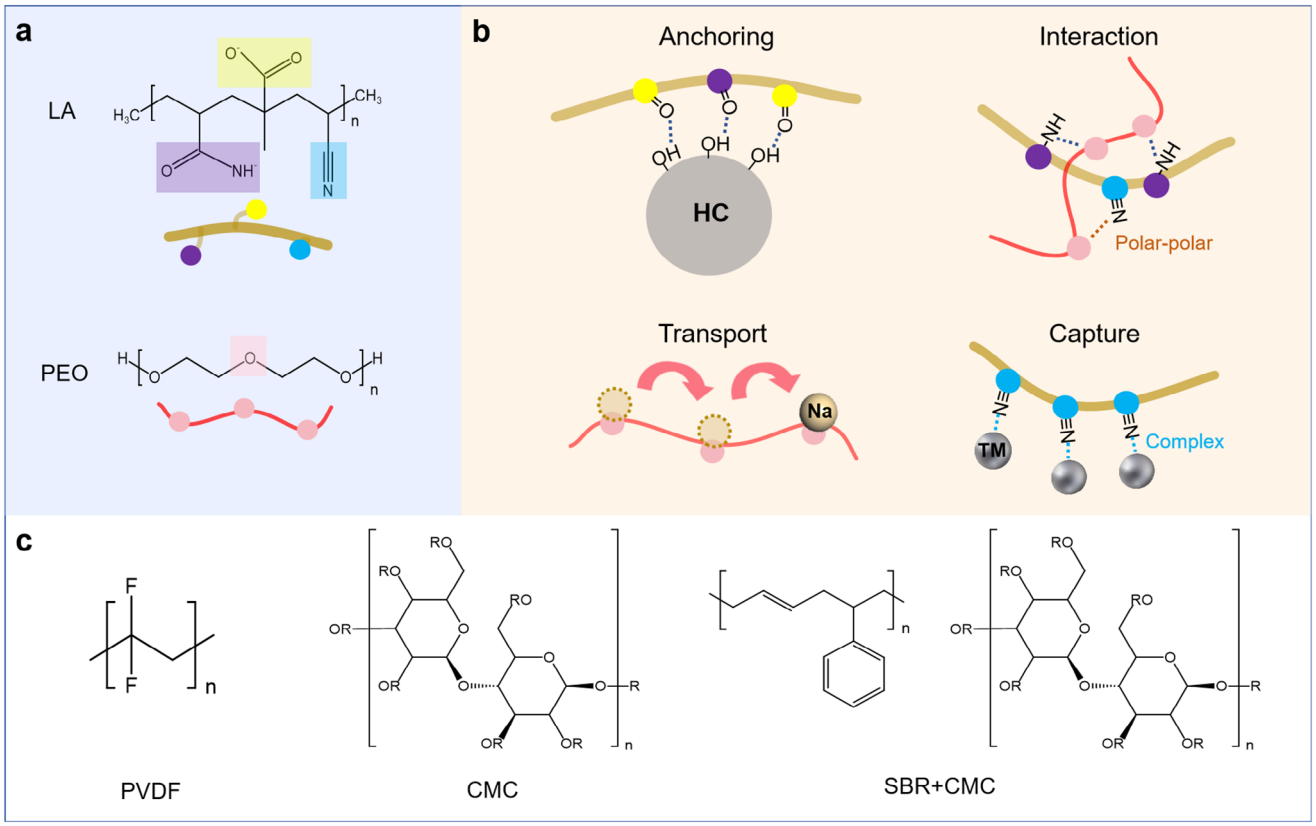

Scheme 1. a) Molecular structures of LA and PEO. b) The role of functional groups in LA/PEO binder. c) Structures of commonly used binders in commerce.

reverse scan, ions can swiftly diffuse back from the electrode surface to the bulk solution, ensuring the efficient discharge process of the battery. These high forward and reverse rates signify that HC-LA/PEO has excellent ion diffusion capabilities as an electrode material. It can promptly respond to external electric field changes and achieve rapid charge–discharge cycles of the battery (Figure 1f; Figures S6 and S7, Supporting Information). Hence, the electrochemical performance suggests that LA/PEO binder possesses a more stable interface structure and faster sodium ion transport efficiency. In addition, HC-LA/PEO also exhibits good charge–discharge performance within a wide temperature range from −20 to 50 °C, demonstrating its potential for applications under extreme operating conditions (Figure 1g). Notably, the electrodes fabricated with this binder demonstrate superior performance in various aspects during electrochemical tests compared to those using other binders (Figure 1h; Table S1, Supporting Information).[33]

Given the small volume changes and high chemical stability of HC during long-cycle charge–discharge processes, it does not cause severe volume expansion and pulverization like silicon-based materials, effectively reducing mechanical damage to the electrodes.[34] However, the inherent problems and interface state of HC significantly impact the electrochemical performance of SIBs.[35] In this context, it is crucial to develop a binder that can not only effectively alleviate the defects and impurities of HC but also improve the interface state. Scanning electron microscopy (SEM) observations found that the surfaces of HC particles using the LA/PEO binder were smoother and more uniform, with no significant voids caused by incomplete coating (**Figure** 2a–c; Figure S8, Supporting Information). It is suggested that the carboxylate group may be an effective anchor point with the HC surface active group, which improves the bond strength between the binder and the active material. When LA is mixed with PEO at a certain ratio, it not only improves the brittleness of LA but also further optimizes the binder's encapsulation of HC particles by forming a uniform coating layer. Fourier-transform infrared (FTIR) spectroscopy analysis on LA/PEO composite and their respective individual component films showed a shift in the O—H stretching vibration peak near 3400 cm^{-1}, indicating the formation of hydrogen bonds between the carboxyl oxygen atoms in LA and the ether oxygen atoms in PEO. Additionally, the intensity of the ether bond stretching vibration peak of PEO at 1100 cm^{-1} has changed and there is a slight shift. Its bond position changes from 1096 to 1103 cm^{-1}, which further confirms the existence of hydrogen bonds (Figure 2d,e).[29] Furthermore, the observed changes in the intensity and position of the C≡N stretching vibration peak suggest the presence of dipole–dipole interactions between the polar cyano groups in LA and the ether oxygen atoms in PEO, indicating that, besides the formation of hydrogen bonds, the polar interaction between the cyano groups in LA and PEO also played a key role in the stability of the overall structure.[14] The strong polarity of the cyano groups promoted intermolecular interactions with surrounding molecules, helping to form a cross-linked network structure between LA and PEO. This

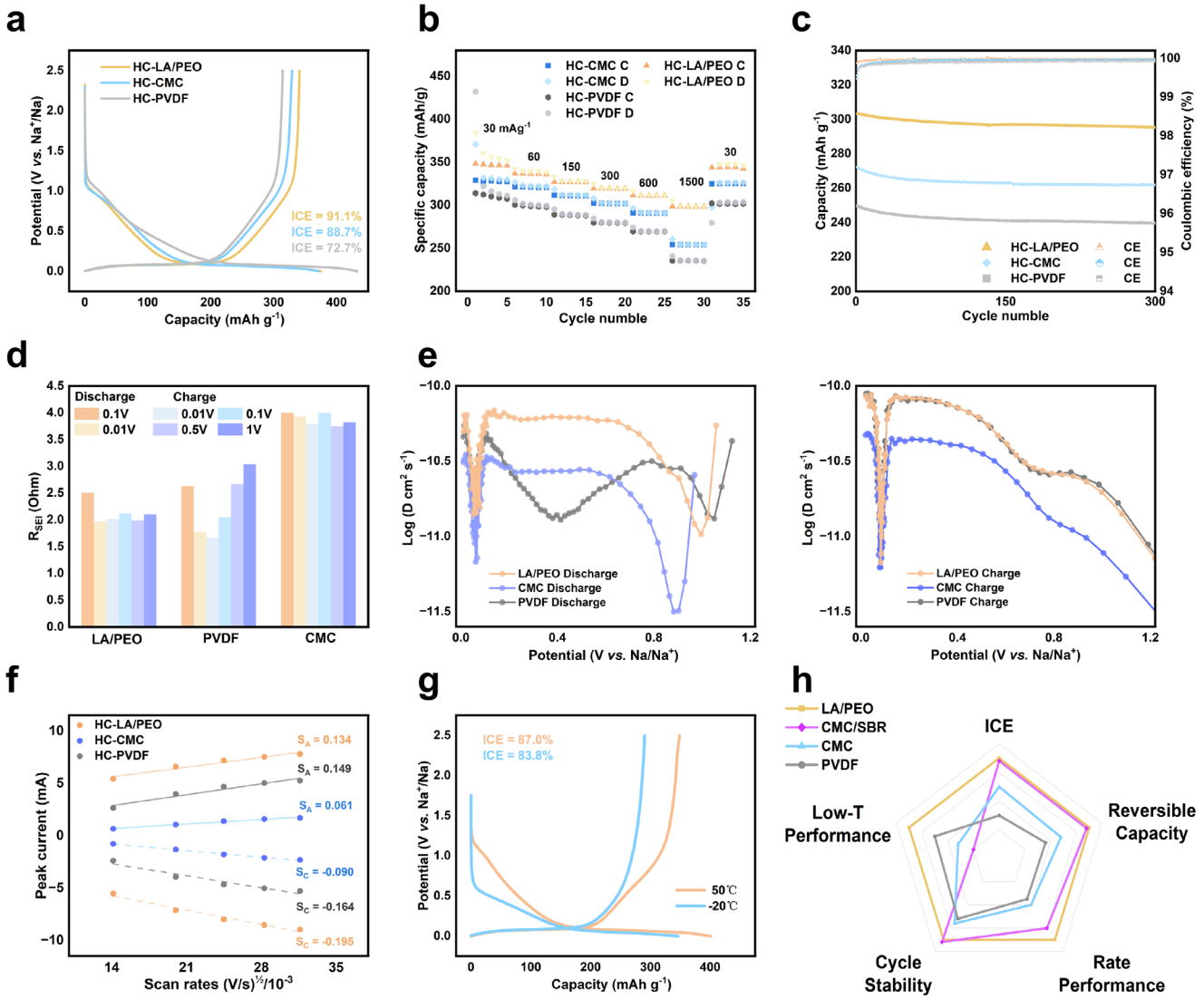

Figure 1. Comparative analyses among binders. a) Galvanostatic charge–discharge curves for the first cycle. b) Rate performance (C:Charge, D:Discharge). c) Cycle performance. d) The change process of R_{SEI} at discharging to 0.1, 0.01 V, and charging to 0.01, 0.1, 0.5, and 1V. e) The sodium-ion diffusion coefficient diagrams of HC-CMC, HC-PVDF, and HC-LA/PEO are calculated from the GITT curves. f) The curves of the relationship between peak current and the square root of the scanning rate. g) Galvanostatic charge–discharge curves for the first cycle under extreme conditions. h) Performance comparison radar chart.

innovative chemical structure not only strengthened the bonding between the binder and the active material but also provided additional chemical crosslinking points, enhancing the overall stability of the electrode materials.[9] This cross-linked structure mitigated the brittleness of HC materials under mechanical shear and contributed to maintaining excellent electronic and ionic conductivity on the electrode surface, which is of great significance for attaining high-performance SIBs. After subjecting the LA and LA/PEO binders to vacuum drying at 100 °C, the resulting powders were utilized for Differential Scanning Calorimetry (DSC) testing. The test results revealed that within the temperature range of 30 to 100 °C a distinct glass-transition temperature was present in LA/PEO, while it was absent in LA (Figure S9, Supporting Information). This property aligns remarkably well with the electrode-preparation technological process. During the fabrication of electrode materials, as the temperature nears the glass-transition temperature of LA/PEO, its molecular segments transition from a relatively immobile glassy state to a highly dynamic rubbery state. This transition significantly enhances the binder's fluidity, enabling LA/PEO to penetrate more effectively into the interstices of the active materials. Consequently, it can proficiently fill and enclose the active substances, thereby strengthening the interaction with the active materials and ultimately optimizing the overall performance of the electrode. Building upon these findings, a tensile-peel test was carried out to assess the adhesion between HC-LA/PEO and the current collector. The test results indicated that the tensile-peel strength of LA/PEO was the highest among the comparative systems (Figure S10, Supporting Information). This elevated tensile-peel strength implies that during the practical operation of the battery, a more stable

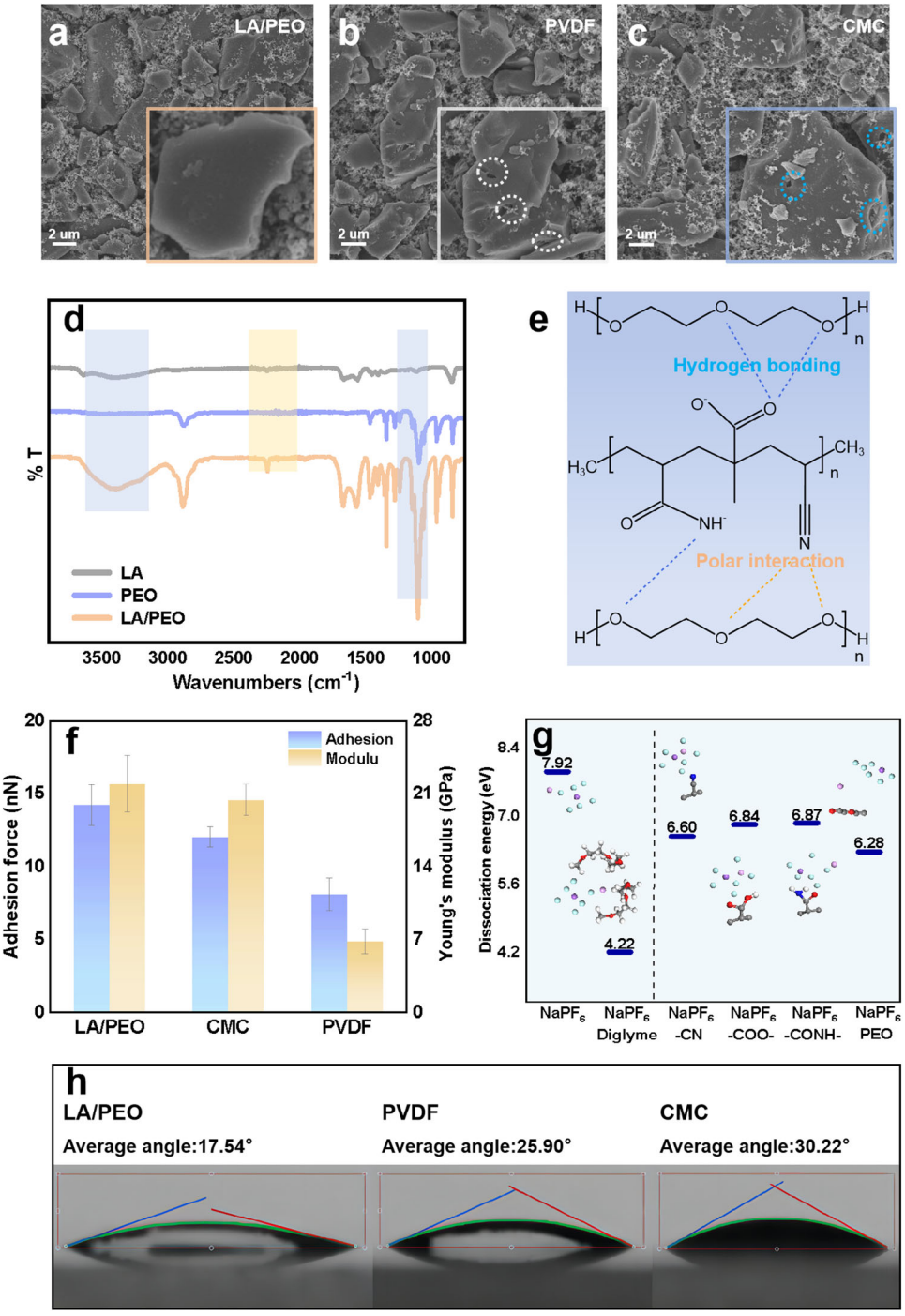

Figure 2. Characterization of binders. Morphology of hard carbon particles encapsulated by a) LA/PEO, b) PVDF, and c) CMC as observed by scanning electron microscopy. d) FT-IR spectra of LA binder, PEO binder, and LA/PEO binder. e) The internal interaction between LA and PEO. f) Adhesion and Young's modulus measured by atomic force microscopy. g) Effect of electrolytes and different groups on the dissociation energy of $NaPF_6$. h) Contact angles of LA/PEO, PVDF, and CMC to DIGLYME electrolyte.

connection can be maintained between the electrode and the current collector. It effectively prevents the electrode from detaching from the current collector due to factors such as vibrations and volume changes occurring during the charging and discharging processes, thus enhancing the battery's cycle life and stability.

To explore the impact of different binders on the mechanical properties of HC electrodes, this study employed atomic force

microscopy (AFM) to test the adhesion force and modulus of binder films spin-coated on glass substrates. The results revealed that LA/PEO binder films exhibited significantly higher adhesion and Young's modulus compared to CMC and PVDF binder films (Figure 2f). This finding indicates that the LA/PEO binder can provide superior mechanical stability for electrodes, crucial for maintaining electrode structure integrity and improving battery cycle stability.[36,37] The calculation based on density functional theory (DFT) showed that the LA/PEO binder could significantly reduce the energy barrier for sodium ion desolvation from the solvated complex to the HC surface, improving the desolvation efficiency of sodium ions and enhancing their orderly arrangement on the electrode surface (Figure 2g; Figure S11, Supporting Information).[29] Contact angle tests further characterized the excellent affinity between LA/PEO films and DIGLYME, with a contact angle of only 17.54°, significantly lower than that of PVDF (25.90°) and CMC (30.22°) films (Figure 2h). The hydrophilicity implies that LA/PEO films can promote sufficient wetting between the electrolyte and electrode materials, thereby enhancing battery charge–discharge efficiency.[38] Moreover, based on the chemical structure similarity between PEO and DIGLYME, we reasonably speculate that this similarity in solvent compatibility can enhance the compatibility between PEO and DIGLYME. This mechanism not only provides a theoretical basis for improving the charge–discharge performance of SIBs but also explains the potential advantages of the LA/PEO binder in all-around battery performance amelioration. Based on the characterization and theoretical calculations, this study suggests that in the electrolyte, Na^+ surrounded by solvent molecules (DIGLYME) can quickly dissociate from the solvent molecules and enter the PEO layer due to the solvent compatibility effect at the interface. The ether oxygen atoms in PEO form coordination bonds with Na^+, stabilizing the sodium ions and promoting their migration and desolvation process. Additionally, the strongly polar cyano groups in LA coordinate with sodium ions, further accelerating Na^+ transfer between binder chains and improving the rate at which sodium ions enter the HC bulk.[39]

After thoroughly analyzing the effects of the LA/PEO binder on the mechanical and electrochemical properties of electrodes, this study also investigated its impact on the characteristics of the SEI film after cycling. By comparing the interface structure and composition of cycled HC anodes treated with different binders, we found that the HC-LA/PEO had significant advantages in SEI film formation. High-resolution transmission electron microscopy (HRTEM) observed that the SEI film formed by HC-LA/PEO was more continuous and uniform and thinner than those of HC-CMC and HC-PVDF (**Figure 3**a–c). Through the analysis of Fast Fourier Transform (FFT) images, the 0.811 nm multilayer stacking corresponding to the NaF (2 2 0) plane was observed, along with lattice spacings corresponding to other inorganic sodium ion compounds (Figure S12, Supporting Information). This further confirmed the thickness and composition of the inorganic layer in the SEI film of HC-LA/PEO, which facilitates efficient sodium ion transport at the interface while reducing electrolyte decomposition, crucial for improving battery cycle stability and long-cycle performance. By analyzing the cross-sectional diagrams of HC after cycling with different binders taken by SEM, it is found that the surface coating of hard carbon particles in HC-LA/PEO is more uniform and thinner (Figure S13, Supporting Information). Based on this, the research believes that a more uniformly dense binder coating will induce the formation of a uniformly dense SEI film. Time-of-flight secondary ion mass spectrometry (TOF-SIMS) analysis disclosed the surface negative ion intensity and depth distribution of the SEI film. When probing the 300 × 300 micrometer electrode sheet surface, it was observed that the negative ion intensity associated with inorganic products was conspicuously lower than that of organic anions. Through the variation curves of negative ion intensities of organic and inorganic products with etching time and the 3D reconstruction model, the superiority of the LA/PEO binder in forming a stable SEI film featuring an inorganic-rich bottom layer and a thin organic upper layer was identified (Figure 3d; Figure S14, Supporting Information). Further, via etching analysis of the electrode sheet after cycling using X-ray photoelectron spectroscopy (XPS), it was detected that the peak intensity of the organic products constituting the SEI on the surface layer was significantly higher than that of the etched electrode sheet, further affirming the composition and distribution of the SEI film at the interface of the electrode sheet (Figure 3e; Figure S15, Supporting Information). Considering the possible swelling of PEO and similar dissipation, it may lead to damage to the structure of the LA/PEO binder, this study subjected HC-LA/PEO to a long-cycle charge–discharge test at 0.6 A g^{-1} for 1000 cycles. The results showed that the capacity retention rate of HC-LA/PEO exceeded 95%, demonstrating excellent cycle stability. Examination of the surface and cross-section of LA/PEO after cycling through triple ion beam cutting and SEM discovered no significant swelling, further confirming the reliability of the LA/PEO binder in practical applications (Figures S16 and S17, Supporting Information).

Although the LA/PEO binder exhibited excellent performance on commercial HC, its application on biomass-derived HC, especially with impurities, is equally critical. Considering the potential presence of metal ion impurities in biomass-derived HC and the potential complexation effect of highly polar cyano (−CN) groups in LA with these metal ions, this study conducted a detailed assessment of the impact of metal ion impurities on the performance of SIBs. Transition metal ion impurities, such as Fe^{3+}, Co^{2+}, Ni^{2+}, and Cu^{2+}, may exist in HC in a free state, potentially triggering unwanted catalytic reactions that negatively affect battery performance.[27] To simulate and study this effect, representative metal ions were selected and doped into commercial HC at different mass ratios (0.1%, 0.5%, 1%) (Figure S18, Supporting Information). Subsequently, high-temperature sintering at 800 °C was conducted to prepare four types of gradient-doped HC samples, named HC-Ctrl (undoped control group) and HC-xM (where x represents the doping ratio and M represents the specific metal element).

Detailed analysis using SEM and transmission electron microscopy combined with energy-dispersive spectroscopy (TEM-EDS) was conducted on the doped HC samples, focusing on the samples with the highest doping levels: HC-0.01Fe, HC-0.01Co, HC-0.01Ni, and HC-0.01Cu. SEM analysis disclosed that merely observing the overall appearance of the electrode did not allow identification of the effects of doped transition metal elements (Figure S19, Supporting Information). At the microscopic scale (micrometer level), there were no significant differences in the appearance of different HC samples. However, TEM-EDS

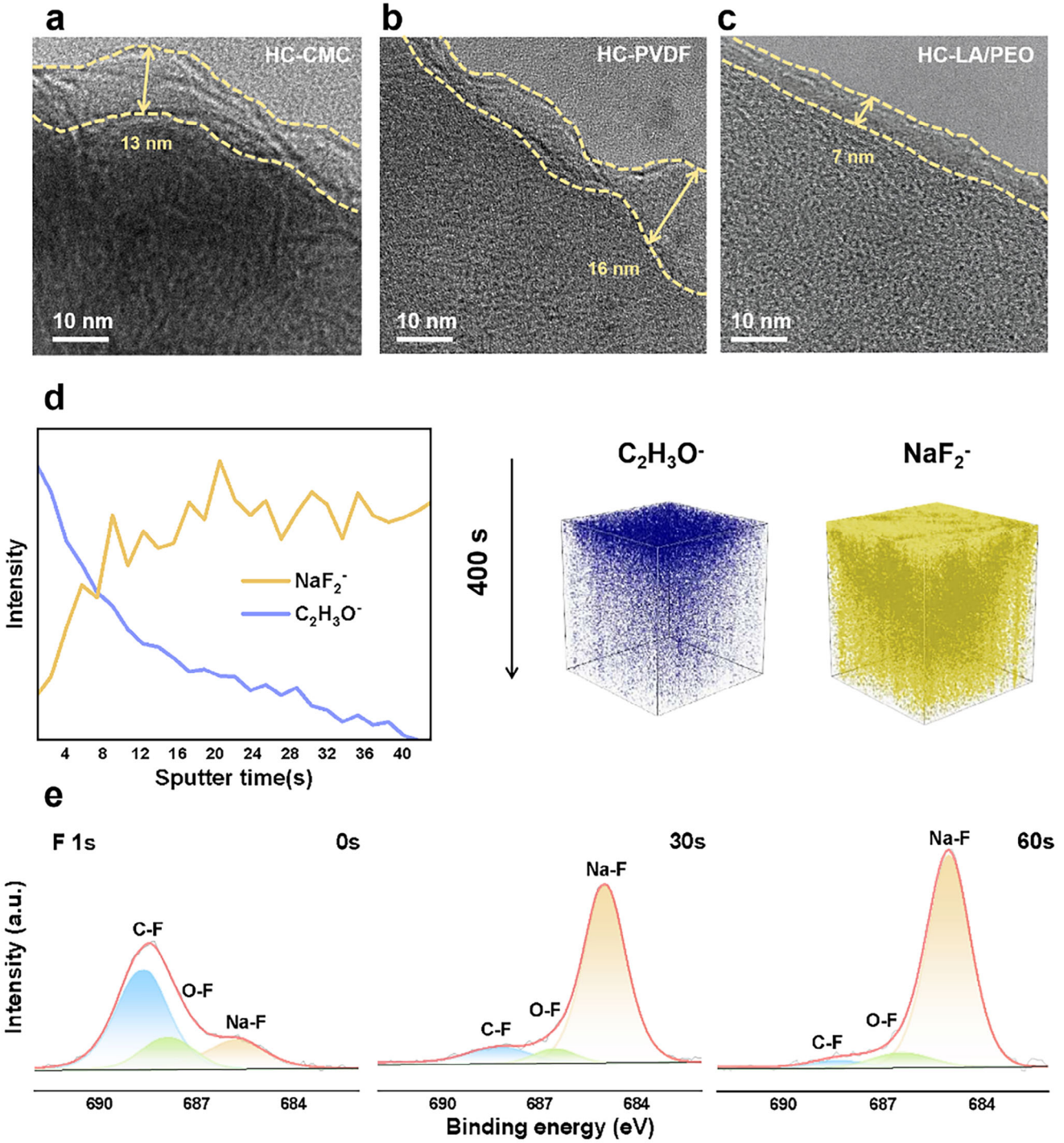

Figure 3. Morphology and structural characterization of SEI films. HRTEM of a) HC-CMC, b) HC-PVDF, and c) HC-LA/PEO. d) High-resolution 3D depth profiles of related ions in a 300 μm × 300 μm area of the HC-LA/PEO electrode after electrochemical cycling. e) XPS spectra of F 1s from HC-LA/PEO, etched for 0, 30 and 60s.

analysis provided deeper insights, unveiling that iron ions were primarily dispersed in the form of iron oxide and iron carbide within the HC matrix, increasing the disorder of the HC. Cobalt ion doping significantly promoted the graphitization process, forming long-range ordered graphitized cage structures in the Co-doped regions, albeit accompanied by defects at the interlayer junctions.[27,40] In contrast, nickel compounds were dispersed in agglomerated spherical forms at the interface, with a relatively minor impact on the HC structure. Copper compound doping also promoted local graphitization but was less significant

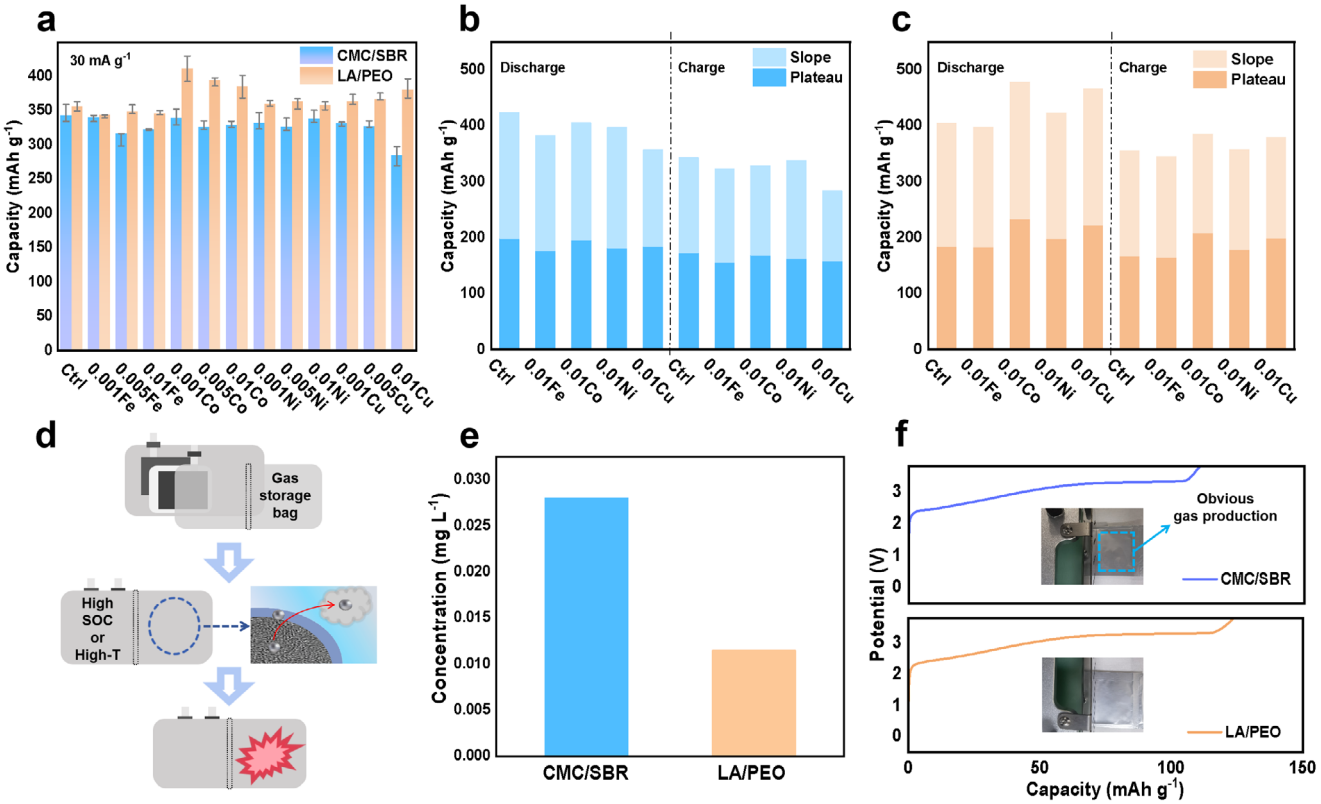

Figure 4. a) Reversible capacity of doped HC at 30 mA g^{-1}. Slope and platform capacity of b) HC-CMC/SBR and c) HC-LA/PEO. d) The influence of TM ions on battery cycling. e) The dissolution situation of TM ions measured by ICP. f) The first-cycle charging curve and gas generation phenomenon of pouch battery.

than cobalt ion doping (Figures S20–S22, Supporting Information). Raman spectroscopy analyses further validated the structural changes. Raman analysis indicated that the dispersed state of iron compounds in the HC-0,01Fe samples reduced the signal intensity, which was consistent with the situation where it affected the structure of HC.[41] All transition metal ion-doped samples showed a decrease in the I(D)/I(G) ratio, attributed to the catalytic effect of transition metal ions on the graphitization of HC. Notably, samples doped with Cu and Co exhibited the most significant decrease in the I(D)/I(G) ratio compared to the control group (0.57 and 0.59 vs 0.71), while Fe-doped samples showed the most pronounced peak shift in the Raman spectra, indicating increased disorder (Figure S23, Supporting Information).[42]

Based on the detailed microstructural analysis, this study categorized the interface characteristics of doped HC samples into four types to elucidate the specific impact of different metal ion doping on the electrochemical performance of HC materials: 1) HC-0.01Fe exhibited limited graphitization in the doped regions with high disorder; 2) HC-0.01Ni retained the pristine microstructure; 3) HC-0.01Cu showed slight graphitization in the doped regions; 4) HC-0.01Co displayed significant graphitization in the doped regions. Electrochemical analysis of these samples revealed that different HC structures effectively showed how binders affected the capacity of batteries with metal ion-doped interfaces.

To verify the practical application effect of the LA/PEO binder, in the subsequent experiments of this study, the commercial CMC/SBR binder, which has better basic electrochemical properties compared with CMC and PVDF, was selected as the comparison standard. Electrochemical characterization of the modified HC mentioned above was also conducted. In rate cycling tests, HC-LA/PEO exhibited generally higher reversible capacity across various rates compared to HC-CMC/SBR, indicating the superior performance of the LA/PEO binder in enhancing the electrochemical performance of HC (Figure S24, Supporting Information). In initial charge–discharge tests, the doped samples with CMC/SBR binder showed stable or reduced initial reversible capacity compared to the undoped control group. Unexpectedly, HC-xCu and HC-xCo samples with LA/PEO binder substantially improved initial reversible capacity. Notably, the HC-xCo sample achieved a high initial reversible capacity of nearly or even beyond 400 mAh g^{-1} during the first charge–discharge, far exceeding conventional performance. In contrast with HC-Ctrl, the charge–discharge capacity of HC-xFe samples decreased significantly. However, the capacity of HC-xNi samples maintained its original level with negligible variation (**Figure 4a**).

Detailed analysis was conducted on the initial charge–discharge curves of the HC-0.01 Mm sample. It was found that whether in the slope region (>0.1 V) or the plateau region (<0.1 V), the capacity loss of the HC sample with the CMC/SBR binder in terms of the charge capacity compared to the discharge capacity was significantly higher than that of the HC sample with the LA/PEO binder (Figure 4b,c).[43,44] This result further confirms the superiority of the LA/PEO binder in

mitigating defects and promoting sodium ion transport kinetics. Additionally, cyclic voltammetry (CV) analysis of electrochemical reactions at the electrode/electrolyte interface revealed that samples with LA/PEO binder exhibited better electrochemical stability and a larger current amplitude, regardless of the highly disordered HC (HC-0.01Fe), HC with minimal structural changes but metal compound aggregation at the interface (HC-0.01Ni), or highly graphitized HC (HC-0.01Cu, HC-0.01Co) (Figure S25, Supporting Information).

After evaluating the electrochemical performance, this study gained a deeper understanding of the role of different binders on metal ion-doped HC interfaces. During high-temperature sintering, despite the reorganization of the microstructure at the interface, the doped transition metal elements (Fe, Co, Ni, Cu) may embed or adsorb in the microscopic pores and interlayer spaces of HC in particulate or ionic forms due to their high affinity with carbon. These metal ions not only act as catalysts to promote the rearrangement and graphitization of carbon atoms but may also form stable metal carbides or strongly interact with surface and internal defects of HC at high temperatures.[27,28] Using the LA/PEO binder, XPS analysis observed shifts in the C 1s peak and corresponding metal peaks, indicating that the highly electronegative cyano groups (—CN) form complexes with free metal ions. Compared to the CMC/SBR binder, the LA/PEO binder showed additional C-metal peaks under the same 30 s etching condition, indicating that X-rays had penetrated the SEI film on the electrode surface to reach the metal carbide-containing HC matrix, further confirming the thinner SEI film formed by the cyano binder (Figure S26, Supporting Information).[45,46] In the industrial context, the presence of iron-ion impurities gives rise to the decomposition of electrolyte and gas generation within batteries under high state-of-charge (SOC) conditions or high-temperature environments, consequently resulting in battery failure (Figure 4d). In light of this problem, this research has conducted inductively coupled plasma (ICP) tests and hot-pressing formation verification on single-layer pouch cells.[47,48] Through ICP testing, the impurity ion content in the electrolyte of the sample doped with 0.5% trivalent iron ions after 300 cycles was confirmed. Specifically, the HC-CMC/SBR contains 0.0280 mg L^{-1} of Fe element, while the HC-LA/PEO contains 0.0115 mg L^{-1} of Fe element. The pouch cells were charged under the pressure of 0.2 MPa and a hot-pressing temperature of 50 °C. The HC-LA/PEO and HC-CMC/SBR were charged to 3.7 V to reach a state with more than 90% SOC (Figure 4e,f; Figure S27, Supporting Information). After standing for thirty days under this temperature and pressure condition, the volume change of the pouch cells was measured by the drainage method. It was found that the gas production of the pouch cell using HC-LA/PEO after hot-pressing formation is significantly lower than that of the pouch cell using HC-CMC/SBR (Figure S27, Supporting Information). In addition, the calculation results also show that the metal ion complex in the LA/PEO binder significantly affects the charge distribution on the electrode surface and the ion distribution in the electrolyte, thereby regulating the interfacial potential and charge transfer rate (Figure S29, Supporting Information). Thus, the study concludes that the stable thin layer formed by the complexes at the electrode surface not only promotes the insertion and extraction of sodium ions but also prevents unnecessary reactions of metal ions on the electrode surface, such as preventing the decomposition of the electrolyte and reducing the irreversible capture of sodium ions by electrode material surfaces.

3. Conclusion

In this study, an LA/PEO composite binder has been developed. Acting as a gatekeeper, the binder effectively enhances the ion transport ability at the hard carbon (HC) interface, mitigating the adverse effects of inherent defects and impurities in biomass-derived hard carbon. This not only showcases its potential in SIBs but also highlights its significance in addressing the challenges faced by the battery industry (**Scheme 2**).

The LA/PEO binder was designed based on the functions of various groups. By forming a uniform and stable SEI layer, it improves the interfacial stability and sodium-ion transport efficiency. The unique chemical structure of the binder further promotes the ion transport rate, enabling the battery to achieve high initial efficiency, reversible capacity, and remarkable rate and long-cycle performance. Moreover, the HC-LA/PEO demonstrates strong tolerance to transition metal ion impurities. This tolerance helps to reduce the negative impact of these impurities on the actual operation of the battery, such as issues related to impurity ion dissolution and gas generation at high temperatures and high state of charge. Compared with the commercial used CMC/SBR binder, the LA/PEO composite binder exhibits priorities in terms of performance and stability, and is expected to achieve a transcendence among most figure of merits, thus providing an alternative binder for commercial hard carbon anodes.

Overall, the LA/PEO composite binder holds great potential in enhancing the performance and stability of SIBs. Its unique design and properties make it a promising solution for improving the efficiency and reliability of SIBs, thereby contributing to the development of the energy storage industry.

4. Experimental Section

Preparation of Hard Carbon Anodes: The hard carbon is of type 2 from Kuraray. The LA133 (Mw ≈ 40–50 W) and PEO (Mw = 110 W) were purchased from Canrud. The HC anodes were prepared by mixing the HC, Super P, and binder in a mass ratio of 8:1:1 in solvent (NMP for PVDF and deionized water for others) to form a series of slurry mixtures. These mixtures were coated onto copper foil and dried at 80 °C for 6 h respectively. Subsequently, each electrode film was cut into 12 mm-discs and placed in a vacuum oven, and baked at 105 °C for 12 h. The mass loading of active materials is ≈1.3–1.9 mg cm^{-2}.

Preparation of $Na_3V_2(PO_4)_3$ (NVP) Cathodes: The NVP was purchased from KEJING (Shenzhen, China). The NVP cathodes were prepared by mixing the NVP, Super P, and LA/PEO (in a weight ratio of 9:1) in a mass ratio of 8:1:1 in water to form a series of slurry mixtures. These mixtures were coated onto Al foil and dried at 80 °C for 6 h respectively. Subsequently, each electrode film was cut into 10 mm-discs and placed in a vacuum oven, and baked at 105 °C for 12 h. The mass of each cathode piece was adjusted to match that of the corresponding anode.

Method of Doping Transition Metal Ions Into the HC: Dissolve transition metal chlorides in deionized water to prepare ionic solutions with a mass fraction of 0.1%. After loading 400 mg of hard carbon into multiple sets of quartz tubes, add the solutions dropwise at different ratios (0.1%, 0.5%, 1%) of the mass of chlorides in the solution to that of the hard carbon to soak the hard carbon. Then, perform ultrasonic dispersion for 6 h and let it stand for 6 h. Subsequently, place the tubes containing the liquid

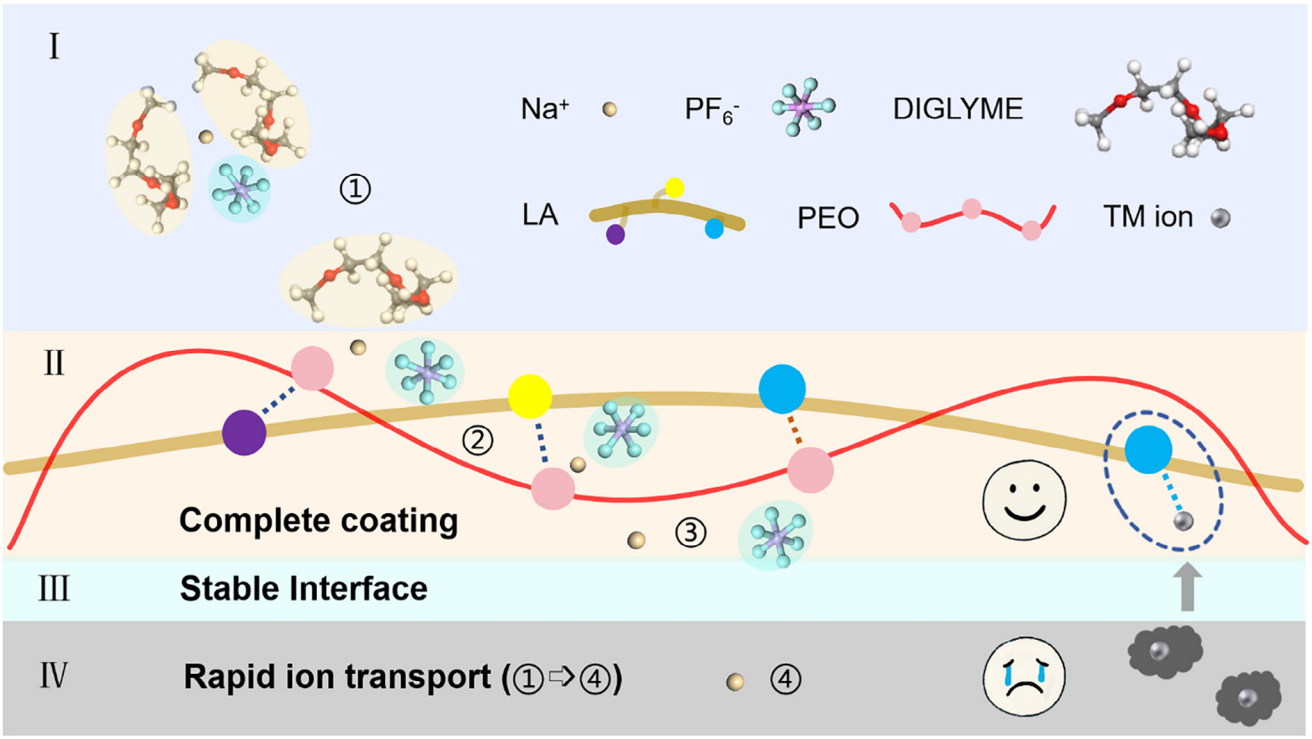

Scheme 2. The effect of the LA/PEO binder at the electrode interface (I:Electrolyte, II:Binder layer, III:SEI layer, IV:Hard carbon).

in a blast oven and dry them at 80 °C for 12 h. After complete drying, put them into a tube furnace, sinter at 800 °C for 6 h, take them out, and grind them into powder for later use.

Materials Characterization: XRD patterns were obtained by X-ray powder diffraction (XRD, Bruker D8 Advance) with Mo Kα radiation (γ = 0.70930 Å) from 10 to 50°using a scan rate of 1° min^{-1}. SEM and TEM were characterized using a scanning electron microscope (SEM, ZEISS Supra 55) and high-resolution field-emission transmission electron microscopy (FETEM) (JEOL-3200FS) equipped with an energy dispersive X-ray spectrometer (EDS). Raman spectra were collected on an inVia Raman microscope (RENISHAW) using an excitation laser beam with a wavelength of 532 nm. Fourier transform infrared spectroscopy (FTIR) was recorded using a Bruker VERTEX 70v spectrometer. The XPS spectra of these electrodes were characterized using X-ray photoelectron spectra (XPS, ESCALAB 250XL). The base pressure of the sample chamber was kept below 3.0 × 10^{-10} mbar. Each specimen was etched with argon ions for 60 s to obtain the interior component information. The obtained emission lines were calibrated by the C 1s signal at 284.8 eV. TOF-SIMS was carried out on a TOF-SIMS instrument (IONTOF M6) equipped with a bismuth primary ion source and an Ar^+ sputter source for probing the fragment ions. The 3D reconstruction graphs of various components were obtained in the area of 300 × 300 µm by using a 30 keV Bi^{3+} primary ion beam, followed by a 1.63 s cycle^{-1} sputter of a 500 × 500 µm area using 1 keV Ar^+ ion beams in an interlaced mode. Inductively Coupled Plasma-Optical Emission Spectroscopy (ICP-OES) analysis was carried out to determine the elemental composition. First, the sample was dissolved in DIGLYME overnight to ensure the complete dissolution of TM ions. Then the dissolved sample was introduced into the ICP-OES instrument.

Electrochemical Measurements: Electrochemical examination was carried out by assembling coin-type (CR2032) half cells and full cells in a high-purity argon-filled glovebox (Mikrouna, Super). In the half cells, 14 mm sodium disks were employed as anodes, 1.0 mol L^{-1} $NaPF_6$ in DIGLYME = 100 Vol% (Dodochem, Suzhou, China) was utilized as the electrolyte, glass fibers (Whatman, GF/C) were adopted as the separator, and hard carbon materials were used as the positive electrode. CHI 660E electrochemical workstation (CH Instruments Inc., China) was employed to measure CV and EIS. Cyclic voltammetry (CV) measurements were conducted at a constant speed of 0.1 mV s^{-1} and a variable speed ranging from 0.2 to 1.2 mV s^{-1} within the voltage range of 0.01 to 2.00 V versus Na^+/Na. Electrochemical impedance spectroscopy (EIS) measurements were performed with an amplitude of 5 mV at frequencies ranging from 100 kHz to 0.1 Hz. The galvanostatic charge/discharge and galvanostatic intermittent titration technique (GITT) tests were conducted using the Netware CT-4008 battery testing system (Shenzhen, China). The pulse and relaxation times of GITT were set to 600 and 3600 s respectively. Galvanostatic charge and discharge measurements were conducted for the half cells within the voltage range of 0.01 to 2.5 V versus Na^+/Na at room temperature, −20, and 50 °C. For the full cells, constant current charge and discharge measurements were carried out within the voltage range of 2.0–4.0 V at room temperature. In the half cells, the amount of electrolyte added was 140 µL. In the full cells, the separator and electrolyte were the same as those in the half cells. The positive and negative electrodes were electrochemically activated in advance for 5 cycles at 0.03 A g^{-1} in the half cells.

Computational Details: Based on density functional theory (DFT) and quantum mechanical calculations, the DMol3 module in the Materials Studio software was employed to compute the dissociation energy and other related parameters. For these specific calculations, the generalized gradient approximation (GGA) was chosen for the exchange-correlation functional, and the Perdew-Wang 1991 (PW91) functional was used for the basis set. All molecular structure optimizations were performed at the GGA/PW91 level, followed by the calculation of dissociation energies and additional parameters.

For the dissociation energy, it is defined as $\Delta E = E_{all} - E_{Na^+} - E_{PF_6^-}$, where E represents the enthalpy of each respective unit.

Equation: Na^+ diffusion coefficients (D_{Na}+)

$$D_{Na^+} = \frac{4}{\pi\tau}\left(\frac{m_B V_m}{M_B S}\right)^2\left(\frac{\Delta E_S}{\Delta E_\tau}\right)^2 \quad (1)$$

where τ (s), m_B (g), M_B (g mol^{-1}), and V_M (mL mol^{-1}) are the pulse duration, the mass, the molar mass, and the molar volume of the active material, namely carbon, respectively. In addition, S (cm^2) is the active area of the working electrode. ΔE_S (V) is the potential difference between two adjacent steady states, and ΔE_τ (V) is the potential change resulting from the pulse current.

Statistical Analysis: Collected data analysis was performed using Origin (2023). For the AFM test results, data were randomly collected from 10 points of the test samples. The results were presented as the mean ± standard deviation (SD), with values accurate to two decimal places. This approach was used to account for the variability within the AFM measurements, considering the variance in sample characteristics at different test points. Regarding the battery data of HC–xM–Binder, the results were obtained from 5 repeated electrochemical tests. To ensure accuracy and better represent the data distribution, the values of key electrochemical parameters such as initial coulombic efficiency (ICE), reversible capacity, and charge–discharge voltage profiles were presented as the median ± extreme values. This method was chosen because it can better capture the spread and central tendency of these battery performance data.

Supporting Information

Supporting Information is available from the Wiley Online Library or from the author.

Acknowledgements

The authors acknowledge the support from the International Joint Research Center for Electric Vehicle Power Battery and Materials (No. 2015B01015), the Guangdong Key Laboratory of Design and Calculation of New Energy Materials (No. 2017B030301013), and the Shenzhen Key Laboratory of New Energy Resources Genome Preparation and Testing (No. ZDSYS201707281026184).

Conflict of Interest

The authors declare no conflict of interest.

Data Availability Statement

The data that support the findings of this study are available in the supplementary material of this article.

Keywords

binder, hard carbon anode, impurity tolerance, interfacial stability, ion transport, sodium-ion batteries

Received: February 11, 2025
Revised: February 26, 2025
Published online: March 11, 2025

[1] C. Vaalma, D. Buchholz, M. Weil, S. Passerini, *Nat. Rev. Mater.* **2018**, *3*, 18013.
[2] N. Sun, J. Qiu, B. Xu, *Adv. Energy Mater.* **2022**, *12*, 2200715.
[3] X. Tang, F. Xie, Y. Lu, H. Mao, Z. Chen, H. Pan, S. Weng, Y. Yang, X. Li, Z. Guo, Q. Guo, F. Ding, X. Hou, Y. Li, X. Wang, M.-M. Titirici, L. Chen, Y. Pan, Y.-S. Hu, *ACS Energy Lett.* **2024**, *9*, 1158.
[4] P. Bai, Y. He, P. Xiong, X. Zhao, K. Xu, Y. Xu, *Energy Storage Mater.* **2018**, *13*, 274.
[5] E. Goikolea, V. Palomares, S. Wang, I. R. de Larramendi, X. Guo, G. Wang, T. Rojo, *Adv. Energy Mater.* **2020**, *10*, 2002055.
[6] L. F. Zhao, Z. Hu, W. H. Lai, Y. Tao, J. Peng, Z. C. Miao, Y. X. Wang, S. L. Chou, H. K. Liu, S. X. Dou, *Adv. Energy Mater.* **2020**, *11*, 2002704.
[7] Y. Chu, J. Zhang, Y. Zhang, Q. Li, Y. Jia, X. Dong, J. Xiao, Y. Tao, Q. H. Yang, *Adv. Mater.* **2023**, *35*, 2212186.
[8] Z. Li, Z. Wu, S. Wu, W. Tang, J. Qiu, T. Liu, Z. Lin, J. Lu, *Adv. Funct. Mater.* **2024**, *34*, 2307261.
[9] J. L. Xia, A. H. Lu, X. F. Yu, W. C. Li, *Adv. Funct. Mater.* **2021**, *31*, 2104137.
[10] Y. Li, A. Vasileiadis, Q. Zhou, Y. Lu, Q. Meng, Y. Li, P. Ombrini, J. Zhao, Z. Chen, Y. Niu, X. Qi, F. Xie, R. van der Jagt, S. Ganapathy, M.-M. Titirici, H. Li, L. Chen, M. Wagemaker, Y.-S. Hu, *Nat. Energy* **2024**, *9*, 134.
[11] Y. Wan, Y. Liu, D. Chao, W. Li, D. Zhao, *Nano Mater. Sci.* **2023**, *5*, 189.
[12] M. Zhang, Y. Li, F. Wu, Y. Bai, C. Wu, *Nano Energy* **2021**, *82*, 105738.
[13] P. Ge, H. Hou, X. Cao, S. Li, G. Zhao, T. Guo, C. Wang, X. Ji, *Adv. Sci.* **2018**, *5*, 1800080.
[14] W. Liu, P. Liu, D. Mitlin, *Adv. Energy Mater.* **2020**, *10*, 2002297.
[15] H. Chen, M. Ling, L. Hencz, H. Y. Ling, G. Li, Z. Lin, G. Liu, S. Zhang, *Chem. Rev.* **2018**, *118*, 8936.
[16] S. Chen, Z. Song, L. Wang, H. Chen, S. Zhang, F. Pan, L. Yang, *Acc. Chem. Res.* **2022**, *55*, 2088.
[17] A. Patra, N. Matsumi, *J. Mater. Chem. A* **2024**, *12*, 11857.
[18] L. Zhong, Y. Sun, K. Shen, F. Li, H. Liu, L. Sun, D. Xie, *Small* **2024**, *20*, 2407297.
[19] S. Wang, J. Yang, W. Cai, G. Wen, S. Yang, K. Ke, B. Yin, X. Fu, W. Yang, Y. Wang, *Adv. Energy Mater.* **2024**, *14*, 2401937.
[20] Z. Su, G. Li, J. Zhang, *Adv. Funct. Mater.* **2024**, *35*, 2415409.
[21] Z. Mao, R. Wang, B. He, J. Jin, Y. Gong, H. Wang, *Small* **2023**, *19*, 2207224.
[22] J. Sheng, Q. Zhang, C. Sun, J. Wang, X. Zhong, B. Chen, C. Li, R. Gao, Z. Han, G. Zhou, *Adv. Funct. Mater.* **2022**, *32*, 4289.
[23] S. Zhou, Z. Tang, Z. Pan, Y. Huang, L. Zhao, X. Zhang, D. Sun, Y. Tang, A. S. Dhmees, H. Wang, *SusMat* **2022**, *2*, 357.
[24] H. Li, C. Guan, J. Zhang, K. Cheng, Q. Chen, L. He, X. Ge, Y. Lai, H. Sun, Z. Zhang, *Adv. Mater.* **2022**, *34*, 2202624.
[25] Y. He, P. Bai, S. Gao, Y. Xu, *ACS Appl. Mater. Interfaces* **2018**, *10*, 41380.
[26] J. Lopez, D. G. Mackanic, Y. Cui, Z. Bao, *Nat. Rev. Mater.* **2019**, *4*, 312.
[27] W. Kiciński, S. Dyjak, *Carbon* **2020**, *168*, 748.
[28] J. Zhao, X. X. He, W. H. Lai, Z. Yang, X. H. Liu, L. Li, Y. Qiao, Y. Xiao, L. Li, X. Wu, S. L. Chou, *Adv. Energy Mater.* **2023**, *13*, 2300444.
[29] W. Li, X. Guo, K. Song, J. Chen, J. Zhang, G. Tang, C. Liu, W. Chen, C. Shen, *Adv. Energy Mater.* **2023**, *13*, 2300648.
[30] S. Chen, X. Wen, Y. Chen, Z. Xia, Q. Chen, L. Huang, H. Huang, H. Pan, Y. Fu, J. He, W. Li, *Chem. Eng. J.* **2024**, *479*, 147813.
[31] D. Bresser, D. Buchholz, A. Moretti, A. Varzi, S. Passerini, *Energy Environ. Sci.* **2018**, *11*, 3096.
[32] W. Huang, Y. Wang, L. Lv, X. Li, Y. Wang, W. Zheng, H. Zheng, *ACS Nano.* **2023**, *17*, 2669.
[33] M. Li, H. Zhuo, Q. Jing, Y. Gu, Z. Liao, K. Wang, J. Hu, D. Geng, X. Sun, B. Xiao, *Carbon Energy* **2024**, *6*, 546.
[34] W. Yan, Z. Mu, Z. Wang, Y. Huang, D. Wu, P. Lu, J. Lu, J. Xu, Y. Wu, T. Ma, M. Yang, X. Zhu, Y. Xia, S. Shi, L. Chen, H. Li, F. Wu, *Nat. Energy* **2023**, *8*, 800.
[35] A. Beda, J.-M. Le Meins, P.-L. Taberna, P. Simon, C. M. Ghimbeu, *Sustainable Mater. Technol.* **2020**, *26*, e00227.
[36] P. Dong, X. Zhang, J. Zamora, J. McCloy, M.-K. Song, *J. Energy Chem.* **2023**, *80*, 442.
[37] Y. Wang, J. Zhu, A. Chen, X. Guo, H. Cui, Z. Chen, Y. Hou, Z. Huang, D. Wang, G. Liang, S. C. Cao, C. Zhi, *Adv. Mater.* **2023**, *35*, 2303165.

[38] Z. Zhang, S. Lu, Y. Li, J. Song, E. Han, H. Wang, Y. He, *Ind. Crops Prod.* **2023**, *203*, 117155.
[39] J. P. Hoffknecht, A. Wettstein, J. Atik, C. Krause, J. Thienenkamp, G. Brunklaus, M. Winter, D. Diddens, A. Heuer, E. Paillard, *Adv. Energy Mater.* **2022**, *13*, 2202789.
[40] Z. Li, C. Bommier, Z. S. Chong, Z. Jian, T. W. Surta, X. Wang, Z. Xing, J. C. Neuefeind, W. F. Stickle, M. Dolgos, P. A. Greaney, X. Ji, *Adv. Energy Mater.* **2017**, *7*, 1602894.
[41] W. Zhu, D. Liu, A. Paolella, C. Gagnon, V. Gariépy, A. Vijh, K. Zaghib, *Front. Energy Res.* **2018**, *6*, 66.
[42] G. M. Bhalerao, M. K. Singh, A. K. Sinha, H. Ghosh, *Phys. Rev. B* **2012**, *86*, 125419.
[43] X. Li, J. Sun, W. Zhao, Y. Lai, X. Yu, Y. Liu, *Adv. Funct. Mater.* **2021**, *32*, 2106980.
[44] H. Kim, J. C. Hyun, D. H. Kim, J. H. Kwak, J. B. Lee, J. H. Moon, J. Choi, H. D. Lim, S. J. Yang, H. M. Jin, D. J. Ahn, K. Kang, H. J. Jin, H. K. Lim, Y. S. Yun, *Adv. Mater.* **2023**, *35*, 2209128.
[45] X. Chen, C. Liu, Y. Fang, X. Ai, F. Zhong, H. Yang, Y. Cao, *Carbon Energy* **2022**, *4*, 1133.
[46] C. Chen, X. Wang, Z. Li, X. Du, Z. Shao, X. Sun, D. Liu, C. Gao, L. Hao, Q. Zhao, B. Zhang, G. Cui, S. Pang, *Angew. Chem., Int. Ed.* **2021**, *61*, 202113932.
[47] Z. Zhang, Z. Cao, T. Zeng, J. Li, M. Jia, J. Liu, Y. Lai, *J. Electrochem. Soc.* **2013**, *160*, A1353.
[48] S. Tang, Y. Liang, Y. Peng, Y. Hu, Y. Liao, X. Yang, H. Zhang, Y. Lin, K. Zhang, J. Liang, B. Li, G. Zhao, Y. Wei, Z. Gong, Y. Yang, *Adv. Energy Mater.* **2024**, *15*, 2402842.